Research Square

Preprints are preliminary reports that have not undergone peer review.
They should not be considered conclusive, used to inform clinical practice,
or referenced by the media as validated information.

Decoding the complex transfer matrix of photonic lanterns

Stephen Eikenberry

stephen.eikenberry@ucf.edu

University of Central Florida https://orcid.org/0000-0002-1332-5061

Miguel Römer

University of Central Florida

Ameer Batarseh

University of Central Florida

Robert Conwell

University of Central Florida

Tara Crowe

University of Central Florida

Caleb Dobias

University of Central Florida https://orcid.org/0009-0000-3311-3165

Swati Bhargava

University of Central Florida

Matthew Cooper

University of Central Florida

Daniel Cruz-Delgado

University of Central Florida

Stephanos Yerolatsitis

University of Central Florida

Sarah Thibaut

University of Central Florida

Kerri Donaldson Hanna

University of Central Florida

Sergio Leon-Saval

The University of Sydney https://orcid.org/0000-0002-5606-3874

Rodrigo Amezcua-Correa

University of Central Florida https://orcid.org/0009-0007-8546-4363

Miguel A. Bandres

University of Central Florida https://orcid.org/0000-0002-7145-8567

Article

Keywords: Photonic Lantern, Image Retrieval, Mode Sorting, Demultiplexing

Posted Date: February 24th, 2026

DOI: https://doi.org/10.21203/rs.3.rs-8444007/v1

License: This work is licensed under a Creative Commons Attribution 4.0 International License.
Read Full License

Additional Declarations: There is **NO** Competing Interest.

Decoding the complex transfer matrix of photonic lanterns

Miguel A. Römer[1†], Ameer B. Batarseh[1†], Robert Conwell[1], Tara Crowe[1], Caleb Dobias[1], Swati Bhargava[1], Matthew Cooper[1], Daniel Cruz-Delgado[1], Stephanos Yerolatsitis[1], Sarah Thibaut[1], Kerri Donaldson Hanna[2,3], Sergio Leon-Saval[4], Rodrigo Amezcua-Correa[1], Miguel A. Bandres[1,3], Stephen S. Eikenberry[1,2,3]

[1]CREOL, The College of Optics & Photonics, University of Central Florida, 4304 Scorpius Street, Orlando, 32816-2700, Florida, USA.
[2]Department of Physics — Planetary Sciences, University of Central Florida, 4111 Libra Drive, Orlando, 32816-2385, Florida, USA.
[3]Florida Space Institute, Florida, USA.
[4]School of Physics, University of Sydney, Australia.

[†]These authors contributed equally to this work.

Abstract

Photonic devices that sort and separate light into spatial modes enable transformative advances in quantum-inspired sub-diffraction imaging, high-fidelity wavefront sensing, free-space optical communication, and quantum information processing. Among these, photonic lanterns offer a compelling solution - efficiently coupling light from a multimode fiber (MMF) into multiple single-mode fibers (SMFs) across a broad wavelength range, facilitating downstream detection and processing. However, effective deployment of photonic lanterns for mode sorting requires knowledge of the full complex transfer matrix—capturing amplitude and phase relationships between MMF modes and SMF outputs. Prior intensity-only approaches fail to recover this essential information. Here we present the first experimental measurement of the complete multimode-to-single-mode complex transfer matrix of a photonic lantern. Using 787 known multimode input fields and a dispersive spectrograph, we reconstruct wavelength-resolved transfer matrices for a 19-port lantern across the 720–880 nm range. We validate the matrices by predicting output intensities for unseen input fields, achieving high

fidelity across all wavelengths. This technique enables full-field utilization of photonic lanterns – including amplitude, phase, polarization, and spectral content – transforming them from intensity couplers into fully calibrated optical interfaces. Precisely modeling the behavior of arbitrary input fields significantly expands the scope of photonic lantern applications to include information-rich imaging and high-capacity communications.

Keywords: Photonic Lantern, Image Retrieval, Mode Sorting, Demultiplexing

1 Introduction

For over a century, the Rayleigh diffraction limit has defined the classical maximum attainable angular resolution in imaging. In traditional "direct" imaging technologies, from human eyes, to cell phone cameras, to the most advanced astronomical telescopes, we examine the intensity of the collected light across a transverse focal plane and find a fundamental limit set by the ratio of the observed wavelength of light divided by the diameter of the light-collecting aperture. In recent years, microscopists have developed techniques for "super-resolution" imaging which can provide angular resolution below the classical diffraction limit, which typically require the use of fluorescent labels, and rely on either structured illumination or pre-conditioned excitation and specialized sample preparation [1–4], thus limiting their operational flexibility and widespread deployment. More recent work has shown that imaging techniques based on spatial modes of light can drive achievable resolution past the classical diffraction limit and even approach the quantum limit for resolution [5, 6]. Importantly, these techniques avoid the requirement for structured illuminating light fields and can provide sub-diffraction super-resolution performance with commonly occurring natural light sources.

A key practical challenge for such modal-basis imaging is the need for a spatial mode sorter: a photonic device that separates different modes of light from a single common input into individual output channels – also known as spatial demultiplexing [7]. A recent technology that has garnered significant research interest for addressing this problem is the photonic lantern (PL): a fiber optic device designed to efficiently transition between a multimode fiber (MMF) and several single-mode fiber (SMF) ports [8, 9]. Lanterns naturally fit the requirements for efficient mode sorting [10, 11]. They are typically made by adiabatically tapering a bundle of N SMF fibers until their cladding forms a new multimode core that supports M spatial LP modes [9, 12], creating an "N-port" photonic lantern where the M-mode input field is uniquely distributed to the N separate channels (Fig 1). Photonic lanterns inherently offer monolithic construction, ease of alignment, high stability, and broad bandwidth. Furthermore, lanterns demonstrate high throughput [13], and scalability, making them a compelling solution compared to other possible mode-sorting technologies (see for instance [14], [15], [16]).

The decoding transfer matrix is a mathematical operator that describes how each of the M supported LP modes in the MMF are converted into the N fundamental modes

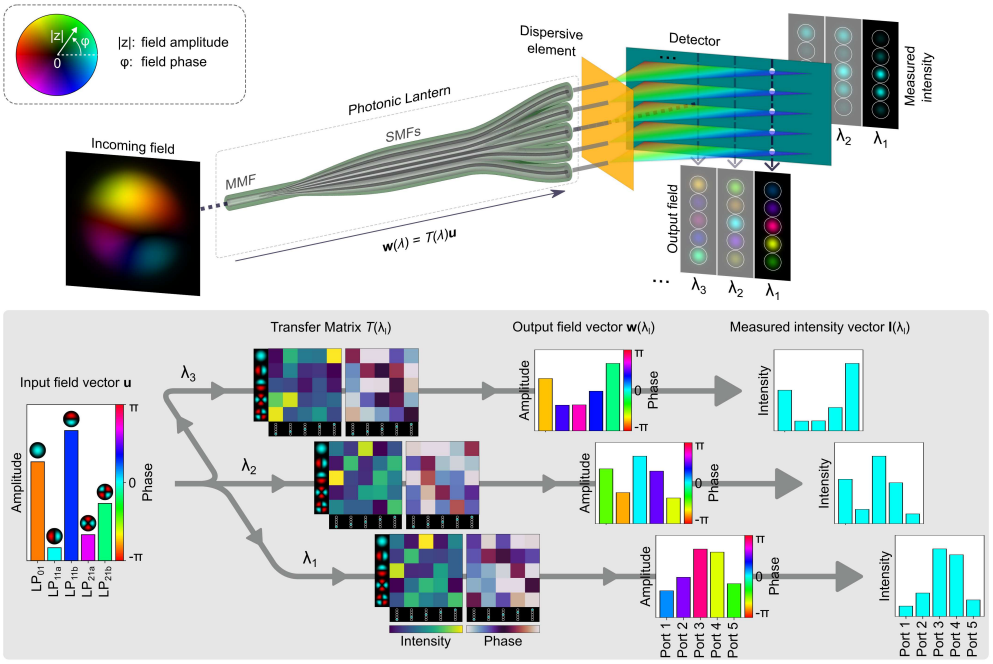


Fig. 1 Operating principle of a photonic lantern for modal imaging. (Top) Flow of light in a photonic lantern system: The input image (a broadband multimode light field, such as produced at the focal plane of a telescope, microscope, or camera) couples into the lantern multimode end, which separates the light into discrete spatial modes corresponding to the single-mode fiber outputs. We arrange the SMF outputs into a linear array and couple their light into a horizontally dispersive spectrograph, which records the intensity spectrum of each mode on a 2-dimensional CMOS detector array. (Bottom) Flow of information: The incoming field consists of a linear combination of the M MMF spatial modes (LP modes), each with its own amplitude and phase, mathematically represented as a complex field vector $\mathbf{u}$. The lantern distributes the light from these modes into the N SMF outputs according to a wavelength-dependent complex transfer matrix T. At each wavelength, the amplitude and phase distribution of the light at the SMF outputs is mathematically represented by the complex vector $\mathbf{w}$, and the spectrograph records their intensities distributed across a vertical detector column as an intensity vector $\mathbf{I}(\lambda)$, with elements $I_j = |w_j|^2$. By reading the intensity values for all ports from each detector column, we can extract the full, wavelength-resolved output data.

of each SMF, with a complex-valued coefficient relating each input mode to each output port. Figure 1 shows the parallel flows of light and modal information through a lantern. For mode-selective photonic lanterns, the transfer matrix is simply a diagonal matrix, because light from a given LP mode on the input MMF side emerges in a single fiber at the SMF output end. However, as the mode count increases, mode-selective lanterns quickly become difficult to manufacture while maintaining good mode selectivity [17], limiting their utility for modal imaging. Conventional (non-mode-selective) photonic lanterns are, in contrast, much easier to scale to larger sizes (see for instance [18], [19], [20]), making them more suitable for practical demultiplexing applications, but also requiring the ability to measure their non-trivial transfer matrices.

Previous matrix-based approaches to characterizing photonic lanterns have been reported, but these typically relate only the *intensities* of the input and output channels, rather than the full complex optical field. Such methods employ real-valued operators—either power transfer matrices, which directly map measured intensities [21–24], or coupling matrices that describe mode-dependent loss in decibels [25–27]. In addition, these studies often assume that the number of supported modes exactly matches the number of output ports ($N = M$), an assumption that does not generally hold for practical lanterns, especially in a broadband regime. These intensity-level matrices are useful for some specific applications, such as when modeling the launch of a single MMF mode at a time, but the lack of phase information prevents them from accounting for the relative phase of each mode, which changes the interactions of the light field inside the PL. In other words, two multimode fields with identical mode amplitudes, but different phases, produce different responses in the device. A full field transfer matrix for each wavelength is therefore required for proper mode-sorting implementations, with complex coefficients relating the amplitudes and phases of the input modes to those of the output ports, as can be seen in Figure 1. Cruz-Delgado et al. [28] simulated such a transfer matrix for a simple 4-port lantern, at a single wavelength, from design parameters, while Tschernig et al. [29] demonstrated efficient simulation of the transfer matrix for a 19-port lantern using the taper reference frame approach. However, a generalized method for experimentally measuring the full decoding transfer matrix of an arbitrary lantern across a large bandwidth has not yet been demonstrated.

We make the distinction between the operator that describes the evolution of light from the multimode end to the single-mode channels, which we call the *decoding* transfer matrix T, and the one that describes the evolution of single-mode light into a multimode channel when the lantern is reversed, the *encoding* transfer matrix B. While this work focuses on the decoding matrix measurement, other authors – for instance [30] and C.D. et. al. (in preparation) – measure the encoding matrix of a lantern (mapping the SMF ports to the MMF end) using off-axis holography. These matrices are true inverses of each other only in the idealized case where the number of modes equals the number of ports ($N = M$); however, as we show here, this is generally not the case. In addition, encoding matrix measurements to-date [30] lack the port-to-port phase coherence needed to obtain the decoding matrix from it. Consequently, one matrix cannot generally be derived from the other.

Here, we demonstrate an experimental technique for obtaining the full decoding transfer matrix of a photonic lantern across a broad wavelength range, allowing its implementation for broadband sources. We measure transfer matrices at ten sample wavelengths between 720 nm and 880 nm for a 19-port conventional lantern by generating a large set of known input fields to feed into the multimode end, and measuring the corresponding wavelength-dependent response at the single-mode end via a dispersive spectrograph. We use the input/output pairs of data at each wavelength to constrain the value of the corresponding transfer matrix, minimizing the difference between the measured output intensities and those predicted by multiplying the known complex input modes with the estimated matrix, and using Jensen-Shannon divergence (JSD) [31] as an evaluation metric. We set aside a subset of measurements as validation data

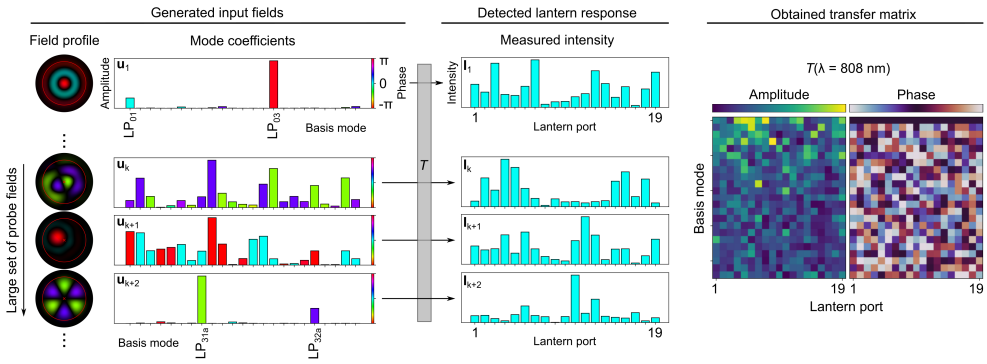


Fig. 2 Transfer Matrix measurement process for a single wavelength, $\lambda = 808$ nm. (Left) We generate a set of several hundred known multimode input fields using a Spatial Light Modulator, each corresponding to a complex mode vector $\mathbf{u}_k$ (coefficients of the supported LP modes). (Middle) Coupling each input field into the photonic lantern propagates the mode vector through the transfer matrix T, producing an intensity response vector $\mathbf{I}_k$ at the PL ports. For a set of input fields that span the available modal space, we can determine the elements of T that map the input modes to output intensities using an optimization algorithm. (Right) Example of a measured transfer matrix (real and imaginary components) for a 19-port lantern at a single wavelength, $T(\lambda = 808\,\text{nm})$. The resulting stochastic ("white noise") appearance is typical in transfer matrices for conventional photonic lanterns.

and do not include them in the transfer matrix estimation, using them to confirm that obtained matrices are successful at predicting the output of the device for a known input.

2 Results

2.1 Measuring the transfer matrix

To demonstrate our method, we use a 19-port photonic lantern tapered from identical single-mode fibers with a design wavelength of 850 nm, labeled PL850. We conduct our analysis for a linear polarization state of $\theta = 0$ for the input light. The lantern features a multimode core diameter of 22.6 μm and a numerical aperture of 0.11. We define the multimode input field as the vector $\mathbf{u}$ (an M-dimensional vector of complex coefficients corresponding to each of the MMF basis modes), as shown in Figure 2 for a selection of probe fields. Similarly, we describe the field in the single-mode output space by arranging N complex coefficients corresponding to the illumination of each of the SMF ports into the vector $\mathbf{w}$, the intensity of which, $\mathbf{I}$, is measured directly. The $N \times M$ transfer matrix T of the lantern linearly maps the input space and the output space as $\mathbf{w} = T\mathbf{u}$ at a given wavelength (vector definitions are further detailed in the Methods section).

We probe the device response by projecting linearly polarized, collimated broadband light onto a Spatial Light Modulator (SLM) to imprint a selected 2-dimensional phase profile at the pupil plane. The polarization state of the field is controlled by rotating a half-wave plate placed after the SLM. This modified wavefront is then imaged onto the multimode end of the photonic lantern. We sequentially generate a

total of 787 probe fields (a number sufficient for a well-posed solution) by utilizing different phase patterns, calculating the corresponding M-element complex input vectors $\mathbf{u}(\lambda)$ for 10 sampled wavelengths between 720 nm and 880 nm. Figure 2 shows a selection of these computed vectors $\mathbf{u}$ at $\lambda = 808\,\text{nm}$, illustrating the varied modal content and phase values. For each probe field, we then measure the resulting output intensities at each wavelength by dispersing the 19 ports through a spectrograph. We present the corresponding output intensity vector measurements $\mathbf{I}(\lambda)$ for these probes at $\lambda = 808\,\text{nm}$ in Figure 2. This process yields a set of 787×10 complex input vectors $\mathbf{u}_k(\lambda_l)$ and a matching set of 787×10 output intensity vectors $\mathbf{I}_k(\lambda_l)$ (with elements $I_j = |w_j|^2$). These pairs of vectors constrain the retrieval of the wavelength-dependent decoding Transfer Matrix, $T(\lambda)$, which for this device is a 19×23 matrix. This non-square dimensionality arises because while the lantern has $N = 19$ single-mode outputs, the multimode fiber core supports $M = 23$ spatial modes across the characterization bandwidth. As noted previously, this mismatch means the matrix cannot be unitary or directly invertible, so the decoding matrix cannot be derived directly from the encoding transfer matrix of the photonic lantern.

We randomly partition the 787 vector pairs into a 90%–10% split, utilizing the larger portion for transfer matrix optimization and reserving the remainder for subsequent validation. These measurements provide sufficient information to determine the ten wavelength-dependent lantern transfer matrices, $T(\lambda_l)$, one for each sampled wavelength. For each case, we compare the measured output – intensity values recorded at the spectrograph – with the predicted output, obtained by applying the estimated TM operator to the input vector. We minimize the mean squared error (MSE) between these two to obtain our transfer matrix operator. The resulting matrix performance is then assessed using the Jensen–Shannon Divergence as a robust evaluation metric, where JSD = 0 indicates perfect agreement between the predicted and measured values. For this lantern, the retrieved matrices achieved a final average JSD of 0.0896 when evaluated on the 90% training set. This represents a high-fidelity result, significantly exceeding the accuracy thresholds required for superresolution imaging, as detailed in the Methods section.

2.2 Validating obtained transfer matrices

To verify the accuracy of our obtained transfer matrices, we examine the 10% of the data reserved for validation. As shown in Fig. 3, we obtain the predicted output vector $\hat{\mathbf{I}}_v(\lambda)$ by multiplying the input vector from the validation set by the previously-determined transfer matrix $T(\lambda)$. We then compare this predicted intensity to the experimentally measured intensity, $\mathbf{I}_v(\lambda)$, using the Jensen-Shannon Divergence metric.

We present the full measured and predicted intensity values across all ports and wavelengths in Figure 3 for three select sample fields, alongside a visualization of their absolute difference and their calculated JSD. For the first field, we also provide a detailed comparison of amplitudes across two different wavelengths, $\lambda = 795$ nm and $\lambda = 808$ nm, which correspond to distinct spectral "slices" of the same broadband input. The measured and predicted values are highly similar throughout the entire validation set, as we can quantify through the JSD values. The final plot in Figure 3

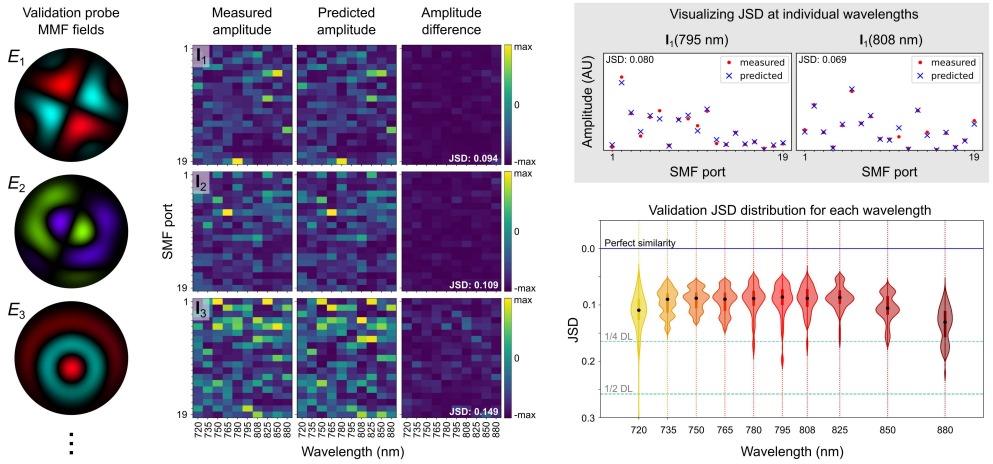


Fig. 3 Transfer Matrix fidelity assessment using independent validation data set. (Left) Three example validation probe fields, along with their corresponding measured intensity vectors at 10 different wavelengths $\mathbf{I}(\lambda)$, and predicted intensity vectors $\hat{\mathbf{I}}(\lambda)$ calculated from the retrieved $T(\lambda)$. We show these as amplitudes $\sqrt{\mathbf{I}}$ to better visualize smaller values. The final column visualizes the absolute amplitude difference, $|\sqrt{\mathbf{I}} - \sqrt{\hat{\mathbf{I}}}|$. (Top right) Detailed comparison of the measured and predicted intensities for probe field E_1 at two adjacent wavelengths, including the calculated Jensen–Shannon Divergence (JSD) metric for these sets of values. (Bottom right) Compiled distributions of the JSD evaluation metric across all validation input fields for each sampled wavelength. Median JSD values are indicated by black dots. Observed JSDs fall consistently below the numerical threshold (indicated by the dashed line) required for one-quarter of the diffraction limit, confirming the high precision of our transfer matrix reconstruction.

compiles the full distribution of observed JSD per validation vector at each sampled wavelength.

We have numerically estimated that the minimum required average JSD across a data set for $0.25\lambda/D$ resolution (a quarter of the diffraction limit) to be 0.165 (see Section 4.3). Our obtained JSD distribution falls consistently below that threshold for all wavelengths. This shows that the transfer matrices we obtain produce predictions that match the observed measurements with very little divergence, well below the maximum tolerable JSD required for $0.25\lambda/D$ resolution imaging. The final average JSD across the entire validation set is 0.0957, notably similar to the value obtained in the training set, confirming the generalizability of our characterization method. We display the entire set of obtained decoding transfer matrices for PL850 in Figure 4.

3 Discussion

We present a general and quantitative framework for determining the full complex-valued decoding transfer matrix of a photonic lantern across a broad wavelength range, demonstrated here on a 19-port PL850 device. By generating a large set of known probe fields in the multimode fiber's intrinsic modal basis and recording their wavelength-resolved responses in the single-mode output basis, we directly reconstruct the multimode-to-single-mode mapping through minimization of the difference between measured and predicted outputs. Validation with independent probe fields

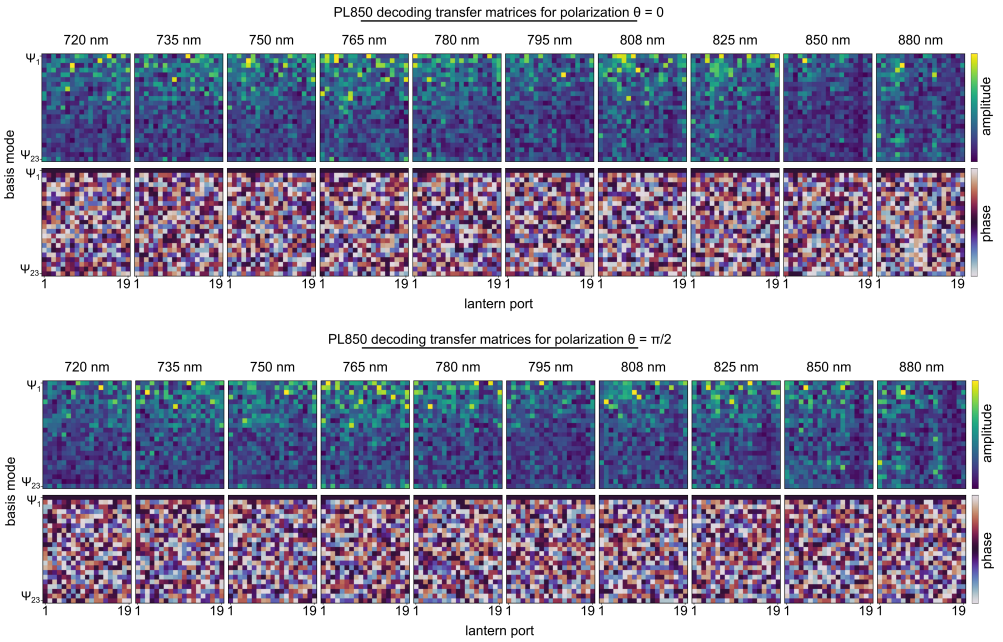


Fig. 4 Broadband complex transfer matrices for the PL850 lantern. Measured decoding transfer matrices, $T(\lambda)$, for PL850 device at each sampled wavelength for the two orthogonal linear polarization states ($\theta = 0$ and $\theta = \pi/2$). Each matrix row corresponds to an LP mode Ψ_i, and each column corresponds to a lantern output port. The final matrix is the operator that minimized the difference between predicted and measured output intensity values. Notably, the matrices show negligible correlation across the sampled wavelengths and between the two orthogonal polarization states, underscoring the necessity of broadband, polarization-resolved characterization.

confirms the effectiveness of this approach, with consistently low JSD values across all ten sampled wavelengths—well below the threshold required for sub-diffraction imaging accuracy.

This technique establishes a new paradigm for the quantitative characterization of multimode photonic interfaces, critical for applications —such as quantum-inspired imaging or wavefront sensing— that require the precise determination of the *decoding* transfer matrix. It extends beyond previous intensity-only models, capturing both amplitude and phase over a broad wavelength range to yield a complete description of device behavior, a necessary approach to accurately account for the device's complex chromatic and polarization-dependent behavior. Crucially, the complex field retrieval is robust because it leverages a diverse set of probe fields that incorporate large phase offsets and spatial discontinuities, unlike techniques limited to small phase perturbations. The ability to obtain broadband, field-resolved transfer matrices transforms photonic lanterns from mere intensity couplers into fully calibrated optical systems. This capability unlocks powerful new applications in high-capacity optical communications, adaptive wavefront control, quantum state manipulation, and information-rich imaging systems.

Our characterization reveals fundamental physical insights into the photonic lantern's behavior, particularly the impact of non-square transfer matrices and the rapid spectral evolution of the device response. In practical lanterns, the number of single-mode ports (N) rarely perfectly matches the number of guided modes (M) across the device's operating bandwidth, resulting in a non-square matrix that represents an intrinsically lossy or over-constrained mapping. This geometric reality, also observed in recent work by Taras et al. [30], means that the encoding and decoding processes are not simple unitary inverses of one another. Furthermore, we observe a significant decorrelation of the transfer matrix across the sampled wavelength range. This "wavelength evolution" confirms that the lantern's modal interference is highly chromatic, a property that necessitates the broadband, field-resolved approach we have demonstrated. These findings re-emphasize that the decoding matrix (T) cannot be reliably derived from encoding matrix measurements (B) through simple pseudo-inversion. Rather, applications requiring high-fidelity field reconstruction need direct characterization of the decoding transfer matrix.

This procedure for measuring the full complex transfer matrix of photonic lanterns, while a significant leap forward, is subject to several practical limitations. The accuracy of the derived matrix is strongly tied to two factors: the precision of the synthesized probe fields and the sensitivity of the output detection system. Any imperfections in generating specific input modes or noise introduced during the measured responses will directly degrade the final matrix fidelity. Furthermore, subtle environmental fluctuations, such as thermal drift during the long measurement sequences, can temporally corrupt the phase relationships and reduce the quality of the results.

From a computational standpoint, the minimization process, though robust, remains susceptible to local minima within the high-dimensional parameter space. This necessitates employing a comprehensive set of probe fields and an efficient optimization algorithm to ensure a reliable global solution is found. Scaling this technique to devices with a significantly higher number of modes or ports presents an increased challenge, as the increase in matrix dimensionality demands a dramatically larger number of probe fields, thereby increasing measurement complexity and duration. Finally, while the achieved precision is sufficient for the stated imaging requirements, its consistent applicability across the full spectrum of photonic lantern designs and operating conditions warrants further validation in future work.

4 Methods

4.1 Mathematical notation

For imaging applications, we orient the photonic lantern such that the shared multimode core is the input, collecting the incoming light fields, and the individual SMF channels are directed toward detectors, which measure the output. Each multimode field $E_{\mathrm{MM}}(x, y)$ that can be guided inside the MMF can be defined by a number M of complex coefficients u_i that describe the amplitude and phase of each mode present

in the field as

$$E_{\mathrm{MM}} = \sum_{i}^{M} u_i \mathbf{\Psi}_i, \tag{1}$$

where $\mathbf{\Psi}_i$ are the orthogonal spatial modes of the MMF (the LP modes) that form the basis of a vector space U. Each coefficient is found as the overlap integral of the total input field and the corresponding basis mode

$$u_i = \frac{\int E^*_{\mathrm{MM}} \mathbf{\Psi}_i dA}{\sqrt{\int |E_{\mathrm{MM}}|^2 dA \int |\mathbf{\Psi}_i|^2 dA}}. \tag{2}$$

The input field is therefore uniquely described by organizing these coefficients into a vector

$$\mathbf{u} = \begin{bmatrix} u_1 \\ u_2 \\ \vdots \\ u_M \end{bmatrix}. \tag{3}$$

Each output field $E_{\mathrm{SM}}(x, y)$ that can be observed on the SMF side is likewise described by N-many complex coefficients w_j that describe the amplitude and phase of the illumination of each port as

$$E_{\mathrm{SM}} = \sum_{j}^{N} w_j \mathbf{G}_j, \tag{4}$$

where $\mathbf{G}_j$ is the fundamental mode of the j^{th} SMF, forming the basis of the output vector space W. The output field is uniquely described by a vector

$$\mathbf{w} = \begin{bmatrix} w_1 \\ w_2 \\ \vdots \\ w_N \end{bmatrix}. \tag{5}$$

We can then define an $N \times M$ operator T that transforms between corresponding vectors in the input space U and the output space W, where the complex element T_{ji} relates the i^{th} MMF mode to the j^{th} SMF port, giving us the equation

$$\mathbf{w} = T\mathbf{u}. \tag{6}$$

This operator is the decoding transfer matrix that describes how a field coupled to the lantern MMF is transformed into the emitted field on the other end. It is important to note that this matrix is different from the encoding transfer matrix B, which relates the fields in the opposite direction with light being joined into the common MMF as $\mathbf{u} = B\mathbf{w}$, which is the matrix measured by [30].

4.2 Constraining the Transfer Matrix

If we consider an estimator $\hat{T} \in \mathbb{C}^{N\times M}$ for the unknown transfer matrix T of the system, the goal is to constrain it until it uniquely matches T (up to a global phase). Each known vector pair $\mathbf{u}_0$ and $\mathbf{w}_0$, related through $\mathbf{w}_0 = T\mathbf{u}_0$, provides a constraint. Thus, our technique relies on synthesizing a set of L multimode fields $\mathbf{u}_k$ (where $k \in \{1,2,...,L\}$) and recording the lantern's corresponding SMF responses, $\mathbf{w}_k$. The set must be large and diverse enough to provide sufficient information about the device behavior, ensuring the problem is not ill-posed and the optimizer can converge to a robust estimator $\hat{T}$.

A primary challenge in determining the minimum number L of vector pairs required to fully determine T is the phase loss upon detection, as we only measure the output intensity vector $\mathbf{I}_k$ (with elements $I_j = |w_j|^2$). This loss of information increases the number of measurements that must be made, as this becomes an NP hard problem [32]. For the phase retrieval problem, a number of distinct measurements $L > 4M - 4$ is typically considered injective [33], ensuring the existence of a unique solution. For practical optimization, we choose a number much larger than this, targeting $L > 10M$ (where $M = 23$ for the PL850). This large, diverse dataset significantly improves the convexity of the loss function, thereby accelerating convergence and enhancing the robustness of the solution. To achieve this diversity and span the input space many times over, we synthesize the 787 unique probe fields using a three-part strategy:

1. Base Fields: We start with 23 base masks, each designed to primarily excite one of the M intrinsic LP modes of the fiber, ensuring all modes are probed at least once.
2. Angular Variation: We introduce additional probe fields by utilizing intermediate rotations of non-circularly-symmetric modes (e.g., intermediate angles between LP_{11a} and LP_{11b} modes).
3. Spatial Offsets: We generate offset versions of these fields by translating the beam relative to the fiber core. More spatial offsets are applied to lower-order modes (which concentrate power near the center), as they still maintain good coupling through small translations.

The final count of $L = 787$ was selected based on numerical simulations showing diminishing returns in convergence acceleration after approximately 700 probe fields, achieving the robustness required while minimizing measurement time. Some examples of these fields and their corresponding input vectors are shown in Fig. 2 for a few examples. This process produces coupling to different modes with diverse phases, which is sufficient to span the input space many times over.

Once we have our full set of vector pairs, we choose a large subset of them (typically 90% of L) to use in optimizing the estimator $\hat{T}$. We find the complex values for each unknown $\hat{T}_{ji}$ such that they produce the minimal possible mean squared difference between the directly measured intensity vector, $\mathbf{I}_k$, and the predicted intensity vector, $\hat{\mathbf{I}}_k$. The predicted vector is obtained from the intensity of each element in $\hat{T}\mathbf{u}_k$: $\hat{I}_{j,k} = |\sum_i \hat{T}_{ji} u_{i,k}|^2$. This difference between the measured and predicted vectors, $\hat{\mathbf{I}}_k - \mathbf{I}_k$, serves as our error in the optimization process, with mean squared error as the loss function to be minimized.

To verify that we have found a general solution, we keep the remaining 10% of vectors for validation; they are not used in the optimization of $\hat{T}$. If our obtained transfer matrix is correct, then for each validation vector, the measured intensity $\mathbf{I}_v$ and the predicted intensity $\hat{\mathbf{I}}_v$ should be near identical. We evaluate the similarity between the two vectors using the Jensen-Shannon Divergence, a symmetric and finite similarity metric based on the Kullback-Leibler divergence, $D(\mathbf{p}, \mathbf{q}) = \sum_i \mathbf{p}_i \log \frac{\mathbf{p}_i}{\mathbf{q}_i}$ [31]. The JSD is defined by

$$\mathrm{JSD}(\mathbf{I}, \hat{\mathbf{I}}) = \frac{1}{2} D(\mathbf{I}, \bar{\mathbf{I}}) + \frac{1}{2} D(\hat{\mathbf{I}}, \bar{\mathbf{I}}), \tag{7}$$

where $\bar{\mathbf{I}} = \frac{1}{2}(\mathbf{I} + \hat{\mathbf{I}})$ represents the average values between the vectors. Two identical vectors will have a JSD of 0, with increasing values representing a greater divergence.

4.3 JSD sensitivity threshold estimation

To quantify how our measured characterization error, measured through JSD, relates to the achievable spatial resolution, we performed a direct simulation. The standard diffraction limit (DL) for our system is defined as DL $\approx \lambda/D$. We calculate the predicted output intensity vectors for two inputs: A known field $E_0(r)$ and the same field shifted spatially by a known amount Δr, $E_{\mathrm{ref}}(r) = E_0(r - \Delta r)$. By multiplying their corresponding input vectors $\mathbf{u}_0$ and $\mathbf{u}_{\mathrm{ref}}$ with our transfer matrices $T(\lambda)$, we calculate the divergence between their produced outputs, $\mathrm{JSD}(\mathbf{I}_0, \mathbf{I}_{\mathrm{ref}})$.

By setting $\Delta r = \frac{1}{4}\lambda/D$ and $\Delta r = \frac{1}{2}\lambda/D$, we obtain reasonable estimates for the maximum JSD threshold that allows us to theoretically resolve elements at these separations. Based on this simulation, we estimate the necessary error thresholds for our system to be JSD < 0.165 for a quarter of the DL, and JSD < 0.258 for half the DL.

4.4 Experimental setup

Our setup for obtaining the transfer matrices of the photonic lantern consists of two main sections: An input field generator that produces the desired multimode fields and feeds them into the lantern's MMF port, and a spectrograph that disperses the single-mode fiber ports, allowing us to record the wavelength-resolved intensity of each.

For the field synthesizer, we take a collimated beam of broadband light from a supercontinuum laser and direct it onto a spatial light modulator. A polarizer enforces the linear polarization state required for SLM interaction, and we impart a phase profile $\phi(x', y')$ on the collimated beam. A subsequent half-wave plate allows us to arbitrarily rotate the polarization axis of the beam. This modulated pupil plane is then focused with a lens to form the image $E(x, y)$ – the field which we couple into the MMF core of the lantern. The decomposition of this focused field into the modes supported by the lantern defines the PL input vector $\mathbf{u}$. We typically perform measurements for two orthogonal linear polarizations of the input light, which we arbitrarily label $\theta = 0$ and $\theta = \pi/2$ and treat independently. We arrange the 19 single-mode output ports of the lantern to form a linear pseudo-slit which is dispersed through a transmissive

grating onto a 2D detector array. This spectrograph can be examined across a given wavelength λ to obtain the 19 intensities that make up the response vector $\mathbf{I}(\lambda)$. Because the input field is broadband, we can use this spectrograph to extract the output vectors for many wavelengths simultaneously.

We typically perform measurements across 10 discrete wavelengths in the range between 720 nm and 880 nm, which is near the design wavelength of the lantern. The dispersive nature of the phase masks used to generate the input modes means that as the wavelength deviates significantly from our chosen reference wavelength of 808 nm (selected to match the monochromatic laser used for initial system alignment), the projected fields begin to fall off the lantern's face, thereby imposing an artificial characterization bandwidth. Choosing a different central phase mask wavelength would allow characterization of the same device in a different regime, and the overall setup is capable of operating in a broader spectral range, approximately 650 nm to 950 nm. Collecting a full data set for each polarization state typically takes on the order of an hour, with the primary time-limiting factor being the data acquisition and handling speed of our spectrograph camera.

Acknowledgments

This material is based upon work supported by the Air Force Office of Scientific Research under award number FA9550-24-1-0332, and the Air Force Grand Challenge in Quantum-Inspired Imaging. The authors also acknowledge support from the University of Central Florida SPICE Academic Excellence Program and the PHAST Jumpstart Initiative.

References

[1] Hofmann, M., Eggeling, C., Jakobs, S., Hell, S.W.: Breaking the diffraction barrier in fluorescence microscopy at low light intensities by using reversibly photoswitchable proteins. Proceedings of the National Academy of Sciences **102**(49), 17565–17569 (2005) https://doi.org/10.1073/pnas.0506010102 https://www.pnas.org/doi/pdf/10.1073/pnas.0506010102

[2] Rust, M.J., Bates, M., Zhuang, X.: Sub-diffraction-limit imaging by stochastic optical reconstruction microscopy (storm). Nature methods **3**(10), 793–796 (2006) https://doi.org/10.1038/nmeth929

[3] Heintzmann, R., Gustafsson, M.G.: Subdiffraction resolution in continuous samples. Nature Photonics **3**(7), 362–364 (2009) https://doi.org/10.1038/nphoton.2009.102

[4] Sigal, Y.M., Zhou, R., Zhuang, X.: Visualizing and discovering cellular structures with super-resolution microscopy. Science **361**(6405), 880–887 (2018) https://doi.org/10.1126/science.aau1044 https://www.science.org/doi/pdf/10.1126/science.aau1044

[5] Tsang, M., Nair, R., Lu, X.-M.: Quantum theory of superresolution for two incoherent optical point sources. Phys. Rev. X **6**, 031033 (2016) https://doi.org/10.1103/PhysRevX.6.031033

[6] Matlin, E.F., Zipp, L.J.: Imaging arbitrary incoherent source distributions with near quantum-limited resolution. Scientific Reports **12**(1), 2810 (2022) https://doi.org/10.1038/s41598-022-06644-3

[7] Richardson, D.J., Fini, J.M., Nelson, L.E.: Space-division multiplexing in optical fibres. Nature photonics **7**(5), 354–362 (2013) https://doi.org/10.1038/nphoton.2013.94

[8] Leon-Saval, S.G., Birks, T.A., Bland-Hawthorn, J., Englund, M.: Multimode fiber devices with single-mode performance. Opt. Lett. **30**(19), 2545–2547 (2005) https://doi.org/10.1364/OL.30.002545

[9] Birks, T.A., Gris-Sánchez, I., Yerolatsitis, S., Leon-Saval, S.G., Thomson, R.R.: The photonic lantern. Adv. Opt. Photon. **7**(2), 107–167 (2015) https://doi.org/10.1364/AOP.7.000107

[10] Fontaine, N.K., Ryf, R., Bland-Hawthorn, J., Leon-Saval, S.G.: Geometric requirements for photonic lanterns in space division multiplexing. Opt. Express **20**(24), 27123–27132 (2012) https://doi.org/10.1364/OE.20.027123

[11] Leon-Saval, S.G., Fontaine, N.K., Salazar-Gil, J.R., Ercan, B., Ryf, R., Bland-Hawthorn, J.: Mode-selective photonic lanterns for space-division multiplexing. Opt. Express **22**(1), 1036–1044 (2014) https://doi.org/10.1364/OE.22.001036

[12] Leon-Saval, S.G., Argyros, A., Bland-Hawthorn, J.: Photonic lanterns. Nanophotonics **2**(5-6), 429–440 (2013) https://doi.org/10.1515/nanoph-2013-0035

[13] Moraitis, C.D., Alvarado-Zacarias, J.C., Amezcua-Correa, R., Jeram, S., Eikenberry, S.S.: Demonstration of high-efficiency photonic lantern couplers for polyoculus. Appl. Opt. **60**(19), 93–99 (2021) https://doi.org/10.1364/AO.424152

[14] Fontaine, N.K., Ryf, R., Chen, H., Neilson, D.T., Kim, K., Carpenter, J.: Laguerre-gaussian mode sorter. Nature communications **10**(1), 1865 (2019) https://doi.org/10.1038/s41467-019-09840-4

[15] Dutton, Z., Kerviche, R., Ashok, A., Guha, S.: Attaining the quantum limit of superresolution in imaging an object's length via predetection spatial-mode sorting. Phys. Rev. A **99**, 033847 (2019) https://doi.org/10.1103/PhysRevA.99.033847

[16] Mirhosseini, M., Malik, M., Shi, Z., Boyd, R.W.: Efficient separation of the orbital angular momentum eigenstates of light. Nature communications **4**(1), 2781 (2013) https://doi.org/10.1038/ncomms3781

[17] Velázquez-Benítez, A.M., Antonio-López, J.E., Alvarado-Zacarías, J.C., Fontaine, N.K., Ryf, R., Chen, H., Hernández-Cordero, J., Sillard, P., Okonkwo, C., Leon-Saval, S.G., *et al.*: Scaling photonic lanterns for space-division multiplexing. Scientific reports **8**(1), 8897 (2018) https://doi.org/10.1038/s41598-018-27072-2

[18] Noordegraaf, D., Skovgaard, P.M.W., Maack, M.D., Bland-Hawthorn, J., Haynes, R., Lægsgaard, J.: Multi-mode to single-mode conversion in a 61 port photonic lantern. Opt. Express **18**(5), 4673–4678 (2010) https://doi.org/10.1364/OE.18.004673

[19] Birks, T.A., Mangan, B.J., Díez, A., Cruz, J.L., Murphy, D.F.: "photonic lantern" spectral filters in multi-core fibre. Opt. Express **20**(13), 13996–14008 (2012) https://doi.org/10.1364/OE.20.013996

[20] Chandrasekharan, H.K., Izdebski, F., Gris-Sánchez, I., Krstajić, N., Walker, R., Bridle, H.L., Dalgarno, P.A., MacPherson, W.N., Henderson, R.K., Birks, T.A., *et al.*: Multiplexed single-mode wavelength-to-time mapping of multimode light. Nature communications **8**(1), 14080 (2017) https://doi.org/10.1038/ncomms14080

[21] Yu, D., Fu, S., Cao, Z., Tang, M., Liu, D., Giles, I., Koonen, T., Okonkwo, C.: Mode-dependent characterization of photonic lanterns. Opt. Lett. **41**(10), 2302–2305 (2016) https://doi.org/10.1364/OL.41.002302

[22] Xu, L., Pei, L., Wang, J., Bai, B., Li, J., Hu, K., Gao, H.: Synthetic photonic lantern characterization and power regulation with intensity superposition mode decomposition. Opt. Express **32**(13), 22663–22674 (2024) https://doi.org/10.1364/OE.523540

[23] Qiu, C., Ma, W., Liu, F., Hu, G.: A simplified mode diversity coherent receiver based on non-mode-selective photonic lantern and kramers-kronig detection. Optics & Laser Technology **161**, 109229 (2023) https://doi.org/10.1016/j.optlastec.2023.109229

[24] Xin, Y., Echeverri, D., Jovanovic, N., Mawet, D., Leon-Saval, S., Amezcua-Correa, R., Yerolatsitis, S., Fitzgerald, M.P., Gatkine, P., Kim, Y.J., *et al.*: Laboratory demonstration of a photonic lantern nuller in monochromatic and broadband light. Journal of Astronomical Telescopes, Instruments, and Systems **10**(2), 025001–025001 (2024) https://doi.org/10.1117/1.JATIS.10.2.025001

[25] Cui, J., Gao, Y., Yang, Y., Ge, D., He, Y., Chen, Z., Li, J.: Design of a highly mode-selective photonic lantern for im/dd mdm transmission. Optics Communications **541**, 129550 (2023) https://doi.org/10.1016/j.optcom.2023.129550

[26] Zhao, L., Li, W., Chen, Y., Yu, T., Zhao, E., Tang, J.: Design and characterization of a self-matching photonic lantern for all few-mode fiber laser systems. Opt. Express **32**(10), 16799–16808 (2024) https://doi.org/10.1364/OE.520588

[27] Dana, Y., Garcia, Y., Kukin, A., Dallachiesa, L., Guerrier, S., Fontaine, N.K., Marom, D.M.: Free-standing microscale photonic lantern spatial mode (de-) multiplexer fabricated using 3d nanoprinting. Light: Science & Applications **13**(1), 126 (2024) https://doi.org/10.1038/s41377-024-01466-6

[28] Cruz-Delgado, D., Alvarado-Zacarias, J.C., Cooper, M.A., Wittek, S., Dobias, C., Martinez-Mercado, J., Antonio-Lopez, J.E., Fontaine, N.K., Amezcua-Correa, R.: Photonic lantern tip/tilt detector for adaptive optics systems. Opt. Lett. **46**(13), 3292–3295 (2021) https://doi.org/10.1364/OL.430761

[29] Tschernig, K., Bhargava, S., Zimmermann, V., Cruz-Delgado, D., Eikenberry, S., Saval, S.L., Correa, R.A., Bandres, M.: Efficient Modeling of Tapered Photonic Structures. Preprint at https://doi.org/10.21203/rs.3.rs-6284889/v1 (2025)

[30] Taras, A.K., Norris, B.R., Betters, C., Ross-Adams, A., Tuthill, P.G., Wei, J., Leon-Saval, S.: Illuminating the lantern: coherent, spectro-polarimetric characterisation of a multimode converter. arXiv preprint arXiv:2510.25330 (2025). Preprint at https://arxiv.org/abs/2510.25330

[31] Lin, J.: Divergence measures based on the shannon entropy. IEEE Transactions on Information theory **37**(1), 145–151 (1991) https://doi.org/10.1109/18.61115

[32] Fickus, M., Mixon, D.G., Nelson, A.A., Wang, Y.: Phase retrieval from very few measurements. Linear Algebra and its Applications **449**, 475–499 (2014) https://doi.org/10.1016/j.laa.2014.02.011

[33] Bandeira, A.S., Cahill, J., Mixon, D.G., Nelson, A.A.: Saving phase: Injectivity and stability for phase retrieval. Applied and Computational Harmonic Analysis **37**(1), 106–125 (2014) https://doi.org/10.1016/j.acha.2013.10.002